

Analysis of evolution of electron-radiation-induced defects in white-luminescent, carbonized, mesoporous silica nanocomposite using transmission electron microscopy/cathodoluminescence

Kazuki Oguni¹, Koji Sato², Yosuke Ishii³, Yukari Ishikawa², Shinji Kawasaki³, Andrii Vasin⁴, Shunsuke Muto^{5*}

¹Graduate School of Engineering, Nagoya University, Nagoya 464-8603, Japan

²Japan Fine Ceramics Center, Nagoya 456-8587, Japan

³Department of Materials Science and Engineering, Nagoya Institute of Technology, Nagoya 466-8555, Japan

⁴Institute of Semiconductor Physics, National Academy of Science of Ukraine, pr. Nauky 41, 03028 Kyiv, Ukraine

⁵Institute of Materials and Systems for Sustainability, Nagoya University, Nagoya 464-8603, Japan

* Corresponding author.

E-mail address: smuto@imass.nagoya-u.ac.jp (Shunsuke Muto)

List of abbreviations:

CL cathodoluminescence

PL photoluminescence

SiOC silicon oxycarbide

MPCS mesoporous carbon-silica

MPS mesoporous silica

TEM transmission electron microscopy

EELS electron energy-loss spectroscopy

STEM scanning transmission electron microscopy

FWHM full width at half maximum

RT room temperature

ODC oxygen deficient center

NBOHC non-bridging oxygen hole center

STE self-trapped exciton

Abstract

We examined the evolution of electron-radiation-induced defects in a white-luminescent, carbonized, mesoporous silica nanocomposite using cathodoluminescence (CL) and electron energy-loss spectroscopy associated with scanning transmission electron microscopy, in order to elucidate the microscopic origins of light emissions in the visible spectral range. The effects of electron irradiation on CL were analyzed based on the differential equations for kinetics of irradiation defects. The nanometric honeycomb silica framework was found to play essentially no role in the electron-excited light emission processes, in contrast to the case for photon-excited processes. The broad and continuous visible emission band in CL consisted of several luminescence components, that have been assigned to optically active point defects such as oxygen-deficient centers, and surface nonbridging oxygen hole centers (NBOHCs) in silica glass.

Keywords: carbonized mesoporous silica, white-light emission, cathodoluminescence, photoluminescence, scanning transmission electron microscopy, electron energy-loss spectroscopy

1. Introduction

White-luminescent materials are being explored widely for use in a range of optical illumination devices, such as light-emitting diodes, plasma displays, and liquid crystal displays [1,2]. Most luminescent materials emit light based on inner-shell transitions in rare earth elements (RE) (Eu and Tb, among others) [3-6] or transition metals (TMs/Cr and Mn, among others) [7-9]. A key characteristic of luminescent materials is the luminescence efficiency, which can be improved significantly by using the appropriate matrix materials, usually metal oxides such as SiAlON, for doping REs [3,4]. However, uncertainties in the supply of REs have highlighted the importance of developing RE-free luminescent materials. Recently, there have been several reports on white luminescence from silicon oxycarbide (SiOC) [10-16], which contains highly abundant elements, namely, Si, O, and C, and is expected to become one of the most suitable white-luminescent materials.

The main drawback of this material is that the photoluminescence (PL) intensity of SiOC is not as strong as that of RE-based phosphors [15,17]. The PL intensity of SiOC seems to increase with the surface area, as some reports have suggested that the PL probably originates at the interface between carbon and silica [15,17]. We have previously reported that mesoporous carbon-silica (MPCS) [16,18,19] with a large surface area emits strong white PL. Further, we have earlier shown that the color-rendering property of the PL and its intensity depend on the hydrolysis and polycondensation reactions that occur during the sol-gel method employed for preparing MPCS [19,20]. These processes can be controlled by regulating the concentration of the acid catalysts used, such as HCl. It is hence expected that SiOC will find use in wall materials, cosmetics, and tooth bleaching, because it is a low-cost and stable material and contains no toxic components.

MPCS exhibits a continuous PL spectrum that covers the visible-light range like solar emission. Further, it is expected that its wide spectrum has several origins [16,18-21]. In addition, it has a broad infrared absorption band at approximately 1100 cm^{-1} and is composed of silica and a small amount of carbon (0.1 wt%) [20,21]. White PL in MPCS nanosilicas was suggested to originate from strained interatomic bonds in silica network [21]. Although, similar broadband PL was observed in carbonized fumed silica and assigned to carbon nanoprecipitates on the surface of silica nanoparticles [22]. It is thus essential to determine how such carbonized silica nanostructures are responsible for light emissions.

In the present study, we examined the local luminescence properties associated with nanometric structural variations using a CL measurement system attached to a transmission electron microscopy (TEM) system. This allowed us to not only probe the light-emission spectrum with submicron spatial resolution but also simultaneously analyze the evolution of the

spectral profiles related to the generation and annihilation of the point defects introduced by high-energy electron irradiation, which changes the electron density and energy. In addition, an electron energy-loss spectroscopy (EELS) system attached to a scanning transmission electron microscopy (STEM) system was used to analyze the local chemistry of the material and map its spatial distribution.

2. Experimental

MPSC nanocomposites were synthesized using a triconstituent co-assembly method [20–21,23]. We used phenol–formaldehyde resin (resol) and tetraethoxysilane (TEOS; Wako, Japan) as the carbon source and silica precursor, respectively. The triblock copolymer Pluronic F127 (Mw = 12600, PEO₁₀₆PO₇₀PEO₁₀₆, Aldrich, USA) was used as the template. A typical synthesis procedure was as follows. First, 8.0 g of Pluronic F127 was dissolved in a solution of 40.0 g of ethanol (EtOH; Nacalai, Japan) and 5.0 g of hydrochloric acid (HCl, Nacalai, Japan) in concentrations ranging from 0.02 to 5 M and stirred for 15 min. Then, 10.4 g of TEOS and 25 g of a 20 wt% ethanolic solution of resol were added to the solution. After the mixture had been stirred at 313 K for 2 h, it was transferred to a Teflon dish. The dish was kept at 313 K for 4 h to evaporate the EtOH. Subsequently, it was kept at 373 K for 15 h to ensure thermopolymerization. Carbonization was carried out in a mullite tubular furnace at 523 K for 3 h (1 K/min) and at 523–873 K (1 K/min), 873–1173 K (5 K/min), and 1173 K for 2 h in N₂. This was followed by cooling to room temperature (RT) at 5 K/min. The carbonized samples were oxidized at 773 K for 6 h (1 K/min) in an air flow and cooled at the same rate to RT. The average pore radii and specific surface areas of the thus-fabricated samples have already been reported [20].

The PL spectra were measured with a conventional photomultiplier at RT using cut excitation light with a filter (for wavelengths shorter than 370 nm). The excitation wavelength was selected as 250 nm using a monochromator combined with a 450 W Xe lamp.

The microstructures of the samples were examined with a TEM system (JEOL JEM-2100 S/TEM) operated at 100 and 200 kV. The STEM-CL measurements were performed using a Gatan Vulcan CL Model 465 system, attached to a STEM system. This system allows the sample to be cooled to approximately 100 K by introducing liquid nitrogen. To prepare the TEM sample, the MPSC sample was ground into a powder with an agate pestle in an agate mortar, and the fine-grained particles were sprinkled on a holey carbon microgrid supported by a copper mesh. Chemical mapping was performed using the spectral imaging technique with an aberration-corrected STEM (AC-STEM) system (JEOL JEM ARM200F S/TEM operated at 80 kV) equipped with an electron energy-loss spectrometer (Gatan GIF Quantum ER).

3. Results

3.1 PL spectra

The PL spectra of the various samples (HCl concentrations of 0.02-5 M during the solution treatment) obtained using a Xe lamp as the excitation light source are shown in Fig. 1. A typical continuous spectrum ranges over the entire visible-light region, confirming white luminescence. The spectrum profile and its center shifted with the HCl concentration during the solution treatment and the carbonization temperature, implying that the color-rendering properties are determined by the sample synthesis conditions, as reported previously [20,21]. In the present study, one of the most luminescent samples, which was synthesized using 0.2 M HCl and which exhibited the best-defined honeycomb framework, was examined further.

3.2 Changes in microstructure and CL spectrum of honeycomb structure with electron irradiation

A representative CL spectrum from a sample particle ($\sim 1 \mu\text{m}$ in size) is shown in Fig. 2(a); the probe size was 300 nm in diameter, the electron current density was 24 A/m^2 at an accelerating voltage of 200 kV, the recording time was 4 s, and the measurement was performed at RT. A high-magnification annular dark-field STEM (ADF-STEM) image of the honeycomb structure is given in Fig. 2(b), which shows scattered sub-nanosized pores besides the larger penetrating pores [21]. The CL spectrum primarily consists of three distinct features, an asymmetric peak at approximately 400–500 nm, a double-peaked component at approximately 600–700 nm, and a central weak feature at 500–600 nm. However, the strongest spectral feature at approximately 500–600 nm in the typical PL spectrum of MPCS is negligibly small. The reason for this is discussed in a later section.

The honeycomb structure was subjected to electron irradiation damage. The microstructural changes induced by electron irradiation at 200 keV at RT are shown together with the associated CL spectrum in Fig. 3, which is a bright-field TEM side view of the honeycomb structure, with the brighter lines corresponding to the pores. Several different areas were examined. It was observed that the initial relative intensities of two of the distinct peak features (asymmetric peak at 400–500 nm and double peak at approximately 600–700 nm) varied from location to location. However, the intensity of each peak varied in a similar manner with time when normalized with respect to the initial intensity. The original honeycomb structure deteriorated gradually with the irradiation time, with the long-wavelength CL component (600–700 nm) shrinking and the central component (500–600 nm) increasing in intensity. Interestingly, the total CL intensity remained almost unaffected with electron irradiation. This implies that the honeycomb structure is not

essential for white-light emission from the investigated material and that the origin of the emission is probably attributable to other sub-nanometer defects, such as point defects.

Hence, we examined the variations in the intensity of the CL as a function of the irradiation time at TEM accelerating voltages of 100 and 200 kV and irradiation temperatures of 100 K and RT (300 K). All the measurements were performed at the same electron current density (22.4 A/m²) and a CL acquisition time of 4 s.

The wide and continuous CL spectrum consisted of several spectral components, as suggested by the results described in the previous section, with each part probably attributable to different types of isolated radiative point defects/complexes, since the shape of the spectral profile (and hence the emission color) changed with changes in the synthesis conditions. Deconvoluting a continuous CL spectrum into its constituent spectral components is not a straightforward task. However, for convenience rather than physical insights, at least five Gaussian components were considered to fit the entire spectrum. Considering how the spectral profile after electron irradiation varied with changes in the accelerating voltage and temperature, the double-peak profile at 600–700 nm was considered a single inseparable component because the intensity of each peak changed in an integrated manner with that of the other. Thus, we instead considered the four independent spectral components shown by the solid lines in Fig. 2(a). The position and full width at half maximum (FWHM) of each component are listed in Table 1.

The change in the intensity of each CL component relative to the initial intensity as a function of the irradiation time is shown in Figs. 4(a)-(d) for the various irradiation temperatures and accelerating voltages. The intensities of components 1 and 4 initially increased dramatically and then decreased asymptotically, while those of components 2 and 3 increased monotonically; this was true for all the irradiation conditions.

3.3 Change in CL intensity of carbon-free mesoporous silica with electron irradiation

To elucidate how carbon is implicated in light emission, the CL spectra of a non-white-luminescent carbon-free mesoporous silicon (MPS) sample were examined. The change in the CL of the MPS sample after electron irradiation at 300 K and an accelerating voltage of 200 kV is shown in Fig. 5. The initial intensity of component #4 was significantly lower than that in the case of the carbonized (MPCS) samples and did not change after electron irradiation. On the other hand, the other components behaved in a manner very similar to that of the carbonized samples after electron irradiation, as described in the previous section. This implies that the former component can either be attributed to a carbon-related defect complex or is produced by the presence of carbon in the samples in the as-synthesized state.

3.4 Chemical mapping by STEM-EELS spectral imaging

To examine the carbon-related defects in further detail, spectral imaging was performed on the MPCs sample using STEM-EELS. The spectral image dataset was obtained using a step width of 0.5 nm and energy dispersion rate of 0.1 eV/channel. The silicon $L_{2,3}$ energy-loss near-edge structures (ELNES) are shown in Fig. 6(a); these correspond to the silica framework and pore surface areas marked 1 and 2 in the ADF-STEM image in Fig. 6(b)). In addition to the standard spectral profile of SiO_2 , the onset of the Si $L_{2,3}$ edge related to the pore surfaces exhibits a small tail structure that extends to the lower energy side; this is attributable to the presence of Si-C or Si-C-O bonds. The spatial distribution map of the Si- O_2 and Si-C (or Si-C-O) bonds originating from the corresponding energy-loss regions is shown in Fig. 6(c), where the Si- O_2 and Si-C (or Si-C-O) bonds are shown in red and green, respectively. It can be seen clearly that the Si-C bonds are localized at the interface between the SiO_2 honeycomb framework as well as in the SiO_2 framework, in keeping with the structural model proposed previously [20,21]. Unfortunately, the carbon K-ELNES could not be obtained for chemical analysis because the carbon contents were estimated to be ~0.2 mass% [20], which is lower than the detection limit for EELS.

4. Discussion

4.1 Assignment of peaks of PL and CL spectra

It is not trivial to be able to map a one-to-one correspondence between the PL and CL spectral components of a luminescent material, because the primary excitation energy, the corresponding energy density, and the subsequent relaxation processes after the electron excitation process for the two phenomena may be very different. Nevertheless, a great deal of data is available on PL/CL emission peaks, which have been summarized in a previous report [24]. According to the listed data table 3.1(a)-(b), by elimination, components #1 and #2 can be assigned to the emission from the self-trapping excitons (STEs) or point defects such as oxygen-deficient centers (ODCs), SiC or Si nanoclusters, and E' centers, considering that their intensities were dependent on the temperature during electron irradiation. Component #3, which had a larger FWHM than those of the other components, exhibited very different intensities in the CL and PL spectra and can be assigned to STEs [24-27] or Si-C nanoclusters [28] or their combinations [29]. Considering that STEs cannot be excited by photons with a wavelength greater than 300 nm [27], their origin as related to the CL and PL spectra would be different. The spectral range of component #4 coincided with the emission from the non-bridging oxygen hole centers (NBOHCs), namely, $(\equiv\text{Si}-\text{O})_3\text{Si}-\text{O}\cdot$ [30,31], and it was reported that the *surface* NBOHC with axial

symmetry gives an energy splitting of about 0.1 eV between the 2p orbitals in the ground state [32]. The explanation given below holds even if the defect geometries assigned to each peak component are not completely correct. It is the chemical properties and mutual behaviors of the luminescent centers that are of importance.

4.2 Components #1 and #2

To explain the time-dependent intensities of the CL spectra corresponding to the different electron irradiation energies and temperatures based on the generation/annihilation of defect complexes by electron irradiation, the reaction kinetics in silica must be considered along with the known radiative point defects complexes and their by-products, as shown in Fig. 7. Since PL studies on silica glass have reported that ODCs or Si nanoclusters and so-called ODCs(II)[33] or dioxasilane ($\equiv\text{Si-O})_2\text{Si}(\text{O}_2)$) [34], result in luminescent peaks at 400–460 nm and 450–470, respectively, we can tentatively assign components #1 and #2 to the ODC variation ($\equiv\text{Si}\cdot\text{Si}\equiv$ (ODCs(I)), and $\equiv\text{Si}\cdot$ (ODCs(II))[33]) since E' centers were reported to emit no luminescence [33] and dioxasilane seems incompatible with the counterpart formation of STEs. Further, if the peak intensities are assumed to be proportional to the concentrations of the corresponding defects, the kinetics rate equations for the reactions in Fig. 7 can be given as follows:

$$\frac{dC_{\text{ODC}}}{dt} = \frac{dC_{\text{IO}}}{dt} = k_1 C_{\text{PR}} - k_{-1} C_{\text{ODC}} C_{\text{IO}} \quad (1)$$

$$\frac{dC_{\text{ODCII}}}{dt} = k_2 C_{\text{PR}} - k_{-2} C_{\text{ODCII}} C_{\text{STE}} \quad (2)$$

$$\frac{dC_{\text{PR}}}{dt} = -(k_1 + k_2) C_{\text{PR}} + k_{-1} C_{\text{ODC}} C_{\text{IO}} + k_{-2} C_{\text{ODCII}} C_{\text{STE}} \quad (3)$$

under the following simplex condition:

$$C_{\text{PR}}^0 + C_{\text{ODC}}^0 + C_{\text{IO}}^0 + C_{\text{ODCII}}^0 + C_{\text{STE}}^0 = C_{\text{PR}} + C_{\text{ODC}} + C_{\text{IO}} + C_{\text{ODCII}} + C_{\text{STE}} = 1 \quad (4)$$

where C_X is the concentration of the species in question ($X = \text{PR}, \text{ODCs}$ (ODC and ODCII for ODCs(I) and ODCs(II), respectively), IO, and STE and represent pristine silica, oxygen-deficient centers, interstitial oxygens, and self-trapped excitons, respectively); C_X^0 is the initial concentration of the species; and k_i is the reaction rate coefficient ($i = \pm 1$ or ± 2 for the two different reaction paths shown in Fig. 7). The minus sign stands for the recovery or inverse reaction.

As shown in Fig. 4, the experimental data could be reasonably well fitted (solid lines) using the least-squares method with a function having the form of the solution of Eqs. (1)–(3):

$$A_i \exp(pt) + B_i \exp(qt) + C_i, \quad i = 1, 2, \quad (5)$$

where $p, q, A_i, B_i,$ and C_i for the fitting parameters the respective irradiation conditions (ODCs(I) and ODCs(II) for $i = 1$ and 2, respectively). The obtained fitting parameters, $p, q, A_i, B_i,$ and C_i

for the various irradiation conditions are listed in Table 1. The derivations of the solutions of Eqs. (1)–(3) are described in Supplementary material 1. To validate the model equations, let us first discuss the reaction rate coefficients, i.e., the k_i values, where k_{-1} alone should exhibit a significant dependence on the temperature because the recovery process involves atomic diffusion while the other electron excitation processes can be ascribed to direct interactions between the incident electrons and the electron system within the material, i.e., the ionic core and outer electrons.

As shown in Supplementary material 2, k_{-2} can be expressed as a function of q , which is almost independent of the irradiation temperature and incident electron energy. This can also be seen from Table 2 and is in keeping with the corresponding process of broken-bond recovery between the ODCs(II) and the STEs through an athermal oxygen exchange relaxation process. On the other hand, the activation energy can be derived from the Arrhenius plot of k_{-1} and is related to the recovery process of the ODCs, as shown in Figs. 8(a) and (b) for incident electron energies of 100 and 200 keV, respectively. Because just two points were available for the plot, the activation energies were estimated to be 0.021 ± 0.007 and 0.01 ± 0.004 eV, respectively, for the electron energies of 100 and 200 keV. It should be noted that these values are lower by two orders of magnitude than the reported activation energies for oxygen diffusion in silica and lower by one order of magnitude than the values derived under high-energy particle irradiation conditions [35]. This difference can be ascribed not only to the enhanced diffusion and incessant generation of broken bonds under the irradiation conditions but also to the fact that the luminescent defects can be recovered by electronic excitation as well as by small, local structural relaxation. These effects are probably by the presence of a small amount of carbon.

In general, the rate coefficient for defect generation by high-energy electron irradiation can be described as the product of the electron flux and the cross-section for defect formation, which should be temperature-independent. As demonstrated in Supplementary material 3, we theoretically predicted the defect generation rates based on the proposed defect formation model and then evaluated the initial defect concentrations, instead of experimentally determining the cross-sections for defect formation, because the light-emission efficiencies for the various peaks were not known. Finally, C_{ODC}^0 and C_{ODCII}^0 were determined for the various irradiation conditions, as shown in Table 3. As expected, the derived initial defect concentrations, C_{ODC}^0 and C_{ODCII}^0 were similar within experimental accuracies for all the conditions, thus further validating the reaction model.

4.3 Component #3

Considering that the recovery process (k_{-2} : Eq. (A-44)) is independent of the temperature,

STEs associated with the point defects, that is, counterparts of the ODCs, can be assumed to be responsible for component #3. Since interstitial oxygen atoms are non-luminescent, a possible defect geometry can be the O-O pairs (an atomistic model for STEs) adjoining the ODCs [26], as shown in Fig. 7.

The experimentally determined time dependence of the peak was fitted using a function of the form $A_3 \exp(pt) + B_3 \exp(qt) + C_3$ and correlated with component #2. The obtained fitting parameters, p , q , A_3 , B_3 , and C_3 for the various irradiation conditions are listed in Table 4. From Eqs. (A-7) and (A-21) in Supplementary material,

$$\begin{aligned} C_{\text{STE}} &= C_{\text{ODCII}}^0 \{A_2 \exp(pt) + B_2 \exp(qt) + C_2\} + C_{\text{STE}}^0 - C_{\text{ODCII}}^0 \\ &= C_{\text{ODCII}}^0 \{A_2 \exp(pt) + B_2 \exp(qt)\} + C_{\text{STE}}^0 - C_{\text{ODCII}}^0 (1 - C_2). \end{aligned} \quad (6)$$

Since $C_{\text{STE}} = C_{\text{STE}}^0 \{A_3 \exp(pt) + B_3 \exp(qt) + C_3\}$,

$$A_3 \exp(pt) + B_3 \exp(qt) + C_3 = \frac{C_{\text{ODCII}}^0}{C_{\text{STE}}^0} \{A_2 \exp(pt) + B_2 \exp(qt)\} + 1 - \frac{C_{\text{ODCII}}^0}{C_{\text{STE}}^0} (1 - C_2). \quad (7)$$

Hence, we obtain the following:

$$A_3 = \frac{C_{\text{ODCII}}^0}{C_{\text{STE}}^0} A_2, \quad B_3 = \frac{C_{\text{ODCII}}^0}{C_{\text{STE}}^0} B_2, \quad C_3 = 1 - \frac{C_{\text{ODCII}}^0}{C_{\text{STE}}^0} (1 - C_2). \quad (8)$$

The experimental data points were best fitted when $C_{\text{ODCII}}^0/C_{\text{STE}}^0 = 0.42$, in keeping with the present model. It should be noted that the ratio $C_{\text{ODCII}}^0/C_{\text{STE}}^0 = 0.42$ should include the ratio of the emission efficiencies of the ODCs(II) and STEs instead of the concentration ratio.

The broad-band-like characteristic of this component can be ascribed to the low relaxation time or partly to the multiple luminescent centers such as SiC nanoclusters associated with the carbonization of the sample. Unfortunately, the change in the intensity of the PL spectrum by electron irradiation was not examined to determine whether this component has the same origin as that of PL band in the same spectral region.

4.4 Component #4

Since this component was the strongest in the case of the carbonized MPS sample in the initial state and the weakest in the non-carbonized MPS sample and did not show time dependence during electron irradiation, it probably places a key in determining the white-luminescent characteristics. Vaccaro et al. [31,32] observed a similar emission peak in the PL spectrum of silica nanoparticles and attributed it to surface NBOHCs.

As can be seen from the curve fitting results in Fig. 4, this component behaves in a very different manner as compared to the other components. The obtained fitting parameters, p , q , A ,

B , and C in the expression $A \exp(pt) + B \exp(qt) + C$ for the various irradiation conditions are listed in Table 5. No emission data for the counterpart of this luminescent center are available to fully explain the change in its intensity with electron irradiation based on a set of differential equations such as Eqs. (1)–(4).

The time dependence of the intensity of component #4 implies that both generation and recovery processes occur during electron irradiation. The initial reaction stage can be treated in the same manner as in Eq. (A-46)–(A-52) in Supplementary material, and the defect generation rate is nearly proportional to $Ap + Bq \sim Aq$, since $Bq \ll Ap$. The fact that a lower electron energy resulted in more defects at a lower temperature suggests that the defects are produced by a radiolysis effect and not by knock-on damage. Moreover, the double-peak nature of this component infers that the present NBOHCs correspond to a surface state, as reported in [32], but the asymmetric geometry is possibly induced by carbon incorporation.

5. Conclusions

In the present study, we examined the evolution of electron-radiation-induced defects in a white-luminescent carbonized, mesoporous silica nanocomposite using TEM-CL and STEM-EELS with the aim of elucidating the microscopic origins of the strong white-light emission, which is similar to solar emission. The time-dependent intensity of the emission under electron irradiation was analyzed based on the reaction kinetics differential equations. The obtained results can be summarized as follows:

1. The nanometric honeycomb silica framework essentially plays no role in the CL phenomenon. It merely increases the relative surface area, leading to the generation of a greater number of carbon-related luminescent centers.
2. The broad, continuous emission band, which is similar to solar emission, consisted of several luminescent components, whose origins could partly be attributed to the luminescent bands attributable to point defects such as oxygen-deficient centers, and surface non-bridging oxygen hole center (NBOHC) defects, as reported in the case of silica glass subjected to various treatments.
3. The broad CL band, observed at 500–700 nm, is probably caused by the self-trapped excitons associated with point defects and surface NBOHCs. The emissions related to these features were likely enhanced by the presence of carbon.

A more detailed analysis of the chemical states of the carbon in the nanocomposite is essential to fully elucidate and understand the mechanism responsible for the observed white luminescence. We are in the process of studying the white luminescence of carbon nanoclusters

decorated on the surfaces of silica particle and will be reporting the results elsewhere.

Acknowledgments

This work was supported in part by a Grant-in-Aid for Scientific Research on Innovative Areas “Nano Informatics” (No. 25106004) and by a Kiban Kenkyu A grant (No. 26249096) from the Japan Society for the Promotion of Science (JSPS). We also thank the DAIKO FOUNDATION for inviting one of the authors (AV) to Nagoya University to collaborate on this work.

References

- [1] Y. Narukawa, M. Ichikawa, D. Sange, M. Sano, and T. Mukai: White light emitting diodes with super-high luminous efficacy, *J. Phys. D: Appl. Phys.* **43** (2010) 354002.
<https://doi.org/10.1088/0022-3727/43/35/354002>.
- [2] C. Feldmann, T. Jüstel, C. R. Ronda, and P. J. Schmidt: Inorganic Luminescent Materials: 100 Years of Research and Application, *Adv. Funct. Mater.* **13** (2003) 511.
<https://doi.org/10.1002/adfm.200301005>
- [3] R. J. Xie, M. Mitomo, K. Uheda, F. F. Xu, and Y. Akimune: Preparation and luminescence spectra of calcium- and rare-earth (R=Eu, Tb, and Pr)-codoped α -SiAlON ceramics, *J. Am. Ceram. Soc.* **85** (2002) 1229. <https://doi.org/10.1111/j.1151-2916.2002.tb00250.x>
- [4] N. Hirosaki, R. Xie, K. Kimoto, T. Sekiguchi, Y. Yamamoto, T. Suehiro, and M. Mitomo: Characterization and properties of green-emitting β -SiAlON: Eu²⁺ powder phosphors for white light-emitting diodes, *Appl. Phys. Lett.* **86** (2005) 211905. <https://doi.org/10.1063/1.1935027>
- [5] G. Adachi: *Kidorui no kagaku (Science of rare earths)* (Kagakudoujin, Kyoto, 1999) p.775 [in Japanese].
- [6] S. Shionoya, W. M. Yen, and H. Yamamoto: *Phosphor Handbook* (CRC Press, Florida, 2006). ISBN 9780849335648
- [7] V. W.-W. Yam, and M.-C. Wong: Luminescent metal complexes of d⁶, d⁸ and d¹⁰ transition metal centres, *Chem. Commun.* **47** (2011) 11579-11592. <https://doi.org/10.1039/C1CC13767K>
- [8] K. K.-W. Lo, and L. J. Charbonnière: Luminescent Materials: Metal Complexes, Clusters, and Nanomaterials, *Eur. J. Chem.* **44** (2017) 5055-5057. <https://doi.org/10.1002/ejic.201701267>
- [9] P. D. Fleischauer and P. Fleischauer: Photoluminescence of transition metal coordination compounds, *Chem. Rev.* **70** (1970) 199-230. <https://doi.org/10.1021/cr60264a002>
- [10] A. Karakuscu, R. Guider, L. Pavesi, and G. D. Soraru: White Luminescence from Sol–Gel - Derived SiOC Thin Films, *J. Am. Ceram. Soc.* **92** (2009) 2969.
<https://doi.org/10.1111/j.1551-2916.2009.03343.x>
- [11] S. Hayashi, M. Kataoka, and K. Yamamoto: Photoluminescence Spectra of Carbon Clusters Embedded in SiO₂, *Jpn. J. Appl. Phys.* **32** (1993) L274-L276.

<https://doi.org/10.1143/JJAP.32.L274>

[12] Y. H. Yu, Y. H. Yu, S. P. Wong, and I. H. Wilson: Visible Photoluminescence in Carbon - Implanted Thermal SiO₂ Films, *Phys. Status Solidi A* **168** (1998) 531-534.

[https://doi.org/10.1002/\(SICI\)1521-396X\(199808\)168:2<531::AID-PSSA531>3.0.CO;2-V](https://doi.org/10.1002/(SICI)1521-396X(199808)168:2<531::AID-PSSA531>3.0.CO;2-V)

[13] J. Zhao, D. S. Mao, Z. X. Lin, B. Y. Jiang, Y. H. Yu, X. H. Liu, H. Z. Wang, and G. Q. Yang: Intense short-wavelength photoluminescence from thermal SiO₂ films co-implanted with Si and C ions, *Appl. Phys. Lett.* **73** (1998) 1838-1840. <https://doi.org/10.1063/1.122299>

[14] S. Y. Seo, K. S. Cho, and J. H. Shin: Intense blue–white luminescence from carbon-doped silicon-rich silicon oxide, *Appl. Phys. Lett.* **84** (2004) 717-719.

<https://doi.org/10.1063/1.1645989>

[15] A. V. Vasin, Y. Ishikawa, N. Shibata, J. Salonen, and V.-P. Lehto: Strong White Photoluminescence from Carbon-Incorporated Silicon Oxide Fabricated by Preferential Oxidation of Silicon in Nano-Structured Si:C Layer, *Jpn. J. Appl. Phys.* **46** (2007) L465-L467.

<https://doi.org/10.1143/JJAP.46.L465>

[16] Y. Ishii, A. Matsumura, Y. Ishikawa, and S. Kawasaki: White Light Emission from Mesoporous Carbon–Silica Nanocomposites, *Jpn. J. Appl. Phys.* **50** (2011) 01AF06.

<https://doi.org/10.1143/JJAP.50.01AF06>

[17] Y. Ishikawa, A. V. Vasin, J. Salonen, S. Muto, V. S. Lysenko, A. N. Nazarov, N. Shibata, and V.-P. Lehto: Color control of white photoluminescence from carbon-incorporated silicon oxide, *J. Appl. Phys.* **104** (2008) 083522. <https://doi.org/10.1063/1.3003079>

[18] A. Matsumura, Y. Ishii, K. Sato, Y. Ishikawa, and S. Kawasaki: White light emitting Mesoporous Carbon-Silica Nanocomposite, *IOP Conf. Ser.: Mater. Sci. Eng.* **18** (2011) 102019. <https://doi.org/10.1088/1757-899X/18/10/102019>

[19] K. Sato, Y. Ishikawa, A. Matsumura, Y. Ishii, and S. Kawasaki: Synthesis of white light emitting mesoporous carbon-silica nanocomposite, *IOP Conf. Ser.: Mater. Sci. Eng.* **18** (2011) 102022. <https://doi.org/10.1088/1757-899X/18/10/102022>

[20] K. Sato, Y. Ishikawa, Y. Ishii, S. Kawasaki, S. Muto, and Y. Yamamoto: Effects of Synthesis Process on Luminescence Properties and Structure of Mesoporous Carbon–Silica Nanocomposite, *Jpn. J. Appl. Phys.* **51** (2012) 082402. <https://doi.org/10.1143/JJAP.51.082402>

[21] Y. Ishikawa, K. Sato, S. Kawasaki, Y. Ishii, A. Matsumura, and S. Muto: White light emission from amorphous silicon-oxycarbide materials, *Phys. Stat. Sol. A* **2019** (2012) 1022-1025. <https://doi.org/10.1002/pssa.201100816>

[22] A. V. Vasin, M. Adlung, V. A. Tertykh, D. Kysil, S. Gallis, A. N. Nazarov, V. S. Lysenko, Broad band (UV-VIS) photoluminescence from carbonized fumed silica: emission, excitation and kinetic properties, *J. Lumin.* **190** (2017) 141–147. <https://doi.org/10.1016/j.jlumin.2017.05.045>

- [23] R. Liu, Y. Shi, Y. Wan, F. Zhang, D. Gu, Z. Chen, B. Tu, and D. Zhao: Triconstituent co-assembly to ordered mesostructured polymer-silica and carbon-silica nanocomposites and large-pore mesoporous carbons with high surface areas, *J. Am. Chem. Soc.* **128** (2006) 11652-62. <https://doi.org/10.1021/ja0633518>
- [24] R. Salh: in *Crystalline Silicon - Properties and Uses* (Ed. By S. Basu), Chapter 8, Defect Related Luminescence in Silicon Dioxide Network: Review, IntechOpen (2011) 135-172. <https://doi.org/10.5772/22607>
- [25] A. N. Trukhin: Self-trapped exciton luminescence in α -quartz, *Nucl. Instr. Meth. Phys. Res. B* **91** (1994) 334-337. [https://doi.org/10.1016/0168-583X\(94\)96242-1](https://doi.org/10.1016/0168-583X(94)96242-1)
- [26] R. T. Williams and K. S. Song: The self-trapped exciton, *J. Phys. Chem. Solids* **51** (1990) 679-716. [https://doi.org/10.1016/0022-3697\(90\)90144-5](https://doi.org/10.1016/0022-3697(90)90144-5)
- [27] D. V. Kysil¹, A. V. Vasin, S. V. Sevostianov, V. Ya Degoda, V. V. Strelchuk¹, V. M. Naseka¹, Yu. P. Piryatinski, V. A. Tertykh, A. N. Nazarov and V. S. Lysenko: Formation and Luminescent Properties of Al₂O₃:SiOC Nanocomposites on the Base of Alumina Nanoparticles Modified by Phenyltrimethoxysilane, *Nanoscale Res. Lett.* **12** (2017) 477. <https://doi.org/10.1186/s11671-017-2245-z>
- [28] W. Hayes, M. J. Kane, O. Salminen, R. L. Wod, and S. P. Doherty: ODMR of recombination centres in crystalline quartz, *J. Phys. C* **17** (1984) 2943-51. <https://doi.org/10.1088/0022-3719/17/16/013>
- [29] X. D. Zhou, F. Ren, X. H. Xiao, J. X. Xu, Z. G. Dai, G. X. Cai, and Z. Ziang: Origin of white light luminescence from Si⁺/C⁺ sequentially implanted and annealed silica, *J. Appl. Phys.* **111** (2012) 084304-1-7. <https://doi.org/10.1063/1.3703668>
- [30] M. A. Lamkin, F. L. Riley, and R. J. Fordham: Oxygen mobility in silicon dioxide and silicate glasses: a review, *J. Eur. Ceram. Soc.* **10** (1992) 347-367. [https://doi.org/10.1016/0955-2219\(92\)90010-B](https://doi.org/10.1016/0955-2219(92)90010-B)
- [31] L. Vaccaro, L. Spallino, S. Agnello, G. Buscarino, and M. Cannas: Defect-related visible luminescence of silica nanoparticles, *Phys. Status Solidi C* **10** (2013) 658-661. <https://doi.org/10.1002/pssc.201200730>
- [32] L. Vaccaro, M. Cannas, V. Radzig, and R. Boscaino: Luminescence of the surface nonbridging oxygen hole center in silica: Spectral and decay properties, *Phys. Rev. B* **78** (2008) 075421. <https://doi.org/10.1103/PhysRevB.78.075421>
- [33] L. Skuja: Optically active oxygen-deficiency-related centers in amorphous silicon dioxide, *J. Non-Cryst. Solids* **239** (1998) 16-48. [https://doi.org/10.1016/S0022-3093\(98\)00720-0](https://doi.org/10.1016/S0022-3093(98)00720-0)
- [34] A. Morana, V. A. Radzig, and M. Cannas: Bright Visible Luminescence in Silica Nanoparticles, *J. Phys. Chem. C* **115**, 19476 (2011). <https://doi.org/10.1021/jp204350u>

- [35] S. Muto, J. Asami and T. Tanabe: RHEED study of irradiation-induced surface damage processes in Si and α -Al₂O₃, Nucl. Instrum. Meth. Phys. Res. B **196** (2002) 324-332. [https://doi.org/10.1016/S0168-583X\(02\)01355-1](https://doi.org/10.1016/S0168-583X(02)01355-1)
- [36] R. A. Johnson and A. N. Orsov (ed.): Physics of Radiation Effects in Crystals, North-Holland, Amsterdam (1986).
- [37] O. Ugurlu, J. Haus, A. Gunawan, M. G. Thomas, S. Maheshwari, M. Tsapatsis, and K. A. Mkhoyan: Radiolysis to knock-on damage transition in zeolites under electron beam irradiation, Phys. Rev. B **83** (2011) 113408. <https://doi.org/10.1103/PhysRevB.83.113408>

Appendix 1. Derivation of solutions of Eqs. (1)–(3)

Since ODCs and IOs are produced in the same amounts during Reaction 1, we get the following from Eq. (1):

$$\begin{aligned} C_{\text{IO}} - C_{\text{ODC}} &= C_{\text{IO}}^0 - C_{\text{ODC}}^0 \\ \therefore C_{\text{IO}} &= C_{\text{ODC}} + C_{\text{IO}}^0 - C_{\text{ODC}}^0. \quad \text{..... (A - 1)} \end{aligned}$$

Similarly, in Reaction 2, since

$$\frac{dC_{\text{ODCII}}}{dt} = \frac{dC_{\text{STE}}}{dt}, \quad (\text{A - 2})$$

we have

$$\begin{aligned} C_{\text{NBOHC}} - C_{\text{ODCII}} &= C_{\text{STE}}^0 - C_{\text{ODCII}}^0 \\ \therefore C_{\text{NBOHC}} &= C_{\text{ODCII}} + C_{\text{STE}}^0 - C_{\text{ODCII}}^0. \quad (\text{A - 3}) \end{aligned}$$

Considering Eqs. (A-1) and (A-3),

$$\frac{dC_{\text{PR}}}{dt} + \frac{dC_{\text{ODC}}}{dt} + \frac{dC_{\text{ODCII}}}{dt} = 0, \quad (\text{A - 4})$$

we have

$$\begin{aligned} C_{\text{PR}} + C_{\text{ODC}} + C_{\text{ODCII}} &= C_{\text{PR}}^0 + C_{\text{ODC}}^0 + C_{\text{ODCII}}^0 \\ \therefore C_{\text{PR}} &= -C_{\text{ODC}} - C_{\text{ODCII}} + C_{\text{PR}}^0 + C_{\text{ODC}}^0 + C_{\text{ODCII}}^0. \quad (\text{A - 5}) \end{aligned}$$

On substituting Eqs. (A-2)–(A-5) in Eqs. (1)–(3), the nonradiative terms are removed, and we obtain the following:

$$\begin{aligned} \frac{dC_{\text{ODC}}}{dt} = \frac{dC_{\text{IO}}}{dt} &= -k_{-1}C_{\text{ODC}}^2 - [(C_{\text{IO}}^0 - C_{\text{ODC}}^0)k_{-1} + k_1]C_{\text{ODC}} - k_1C_{\text{ODCII}} \\ &+ k_1(C_{\text{PR}}^0 + C_{\text{ODC}}^0 + C_{\text{ODCII}}^0) \quad (\text{A - 6}) \end{aligned}$$

$$\begin{aligned} \frac{dC_{\text{ODCII}}}{dt} = \frac{dC_{\text{STE}}}{dt} &= -k_{-2}C_{\text{ODCII}}^2 - [(C_{\text{STE}}^0 - C_{\text{ODCII}}^0)k_{-2} + k_2]C_{\text{ODCII}} - k_2C_{\text{ODC}} \\ &+ k_2(C_{\text{PR}}^0 + C_{\text{ODC}}^0 + C_{\text{ODCII}}^0) \quad (\text{A - 7}) \end{aligned}$$

$$\begin{aligned} \frac{dC_{\text{PR}}}{dt} &= k_{-1}C_{\text{ODC}}^2 + k_{-2}C_{\text{ODCII}}^2 + (C_{\text{IO}}^0 - C_{\text{ODC}}^0)k_{-1}C_{\text{ODC}} + (C_{\text{STE}}^0 - C_{\text{ODCII}}^0)k_{-2}C_{\text{ODCII}} \\ &+ (k_1 + k_2)(C_{\text{ODC}} + C_{\text{ODCII}}) - (k_1 + k_2)(C_{\text{PR}}^0 + C_{\text{ODC}}^0 + C_{\text{ODCII}}^0) \quad (\text{A - 8}) \end{aligned}$$

Since the amounts of point defect complexes in silica should be small compared to the amounts of the main silica building units, the quadratic terms such as C_{ODC}^2 and C_{ODCII}^2 can be neglected. Further, $C_{\text{PR}}^0 + C_{\text{ODC}}^0 + C_{\text{ODCII}}^0 \approx C_{\text{PR}}^0$, and Eqs. (A - 6) and (A - 7) can be rewritten as:

$$\frac{dC_{\text{ODC}}}{dt} = -[(C_{\text{IO}}^0 - C_{\text{ODC}}^0)k_{-1} + k_1]C_{\text{ODC}} - k_1C_{\text{ODCII}} + k_1C_{\text{PR}}^0, \quad (\text{A - 9})$$

$$\frac{dC_{\text{ODCII}}}{dt} = -[(C_{\text{STE}}^0 - C_{\text{ODCII}}^0)k_{-2} + k_2]C_{\text{ODCII}} - k_2C_{\text{ODC}} + k_2C_{\text{PR}}^0. \quad (\text{A} - 10)$$

The simultaneous differential equations (A-9) and (A-10) can be solved readily. The solutions are expressed as linear combinations of two exponential terms (the generation and annihilation terms, respectively) as follows:

$$C_{\text{ODC}} = \frac{1}{2}\left(L_1 - \frac{M_1}{\sqrt{Y}}\right) \exp\left(\frac{X - \sqrt{Y}}{2}t\right) + \frac{1}{2}\left(L_1 + \frac{M_1}{\sqrt{Y}}\right) \exp\left(\frac{X + \sqrt{Y}}{2}t\right) + N_1 \quad (\text{A} - 11)$$

$$C_{\text{ODCII}} = \frac{1}{2}\left(L_2 - \frac{M_2}{\sqrt{Y}}\right) \exp\left(\frac{X - \sqrt{Y}}{2}t\right) + \frac{1}{2}\left(L_2 + \frac{M_2}{\sqrt{Y}}\right) \exp\left(\frac{X + \sqrt{Y}}{2}t\right) + N_2 \quad (\text{A} - 12)$$

where

$$X = -[(C_{\text{IO}}^0 - C_{\text{ODC}}^0)k_{-1} + k_1 + (C_{\text{STE}}^0 - C_{\text{ODCII}}^0)k_{-2} + k_2], \quad (\text{A} - 13)$$

$$Y = X^2 - 4K, \quad (\text{A} - 14)$$

$$K = (C_{\text{IO}}^0 - C_{\text{ODC}}^0)(C_{\text{STE}}^0 - C_{\text{ODCII}}^0)k_{-1}k_{-2} + (C_{\text{IO}}^0 - C_{\text{ODC}}^0)k_{-1}k_2 + (C_{\text{STE}}^0 - C_{\text{ODCII}}^0)k_1k_{-2}, \quad (\text{A} - 15)$$

$$L_1 = C_{\text{ODC}}^0 - N_1, \quad (\text{A} - 16)$$

$$M_1 = \{X + 2[(C_{\text{STE}}^0 - C_{\text{ODCII}}^0)k_{-2} + k_2]\}L_1 - 2k_1L_2, \quad (\text{A} - 17)$$

$$N_1 = \frac{C_{\text{PR}}^0(C_{\text{STE}}^0 - C_{\text{ODCII}}^0)k_1k_{-2}}{K}, \quad (\text{A} - 18)$$

$$L_2 = C_{\text{ODCII}}^0 - N_2, \quad (\text{A} - 19)$$

$$M_2 = \{X + 2[(C_{\text{IO}}^0 - C_{\text{ODC}}^0)k_{-1} + k_1]\}L_2 - 2k_2L_1 \quad (\text{A} - 20),$$

and

$$N_2 = \frac{C_{\text{PR}}^0(C_{\text{IO}}^0 - C_{\text{ODC}}^0)k_{-1}k_2}{K}. \quad (\text{A} - 21)$$

The experimental data could thus be reasonably well fitted by the least-squares method using a

function of the form

$$A_i \exp(pt) + B_i \exp(qt) + C_i, \quad i = 1, 2 \quad (\text{A-22})$$

and the simplified forms of Eqs. (A-11) and (A-12) with the corresponding relations:

$$\frac{X - \sqrt{Y}}{2} = -p, \quad \frac{X + \sqrt{Y}}{2} = -q, \quad (\text{A-23})$$

$$\frac{1}{2} \left(L_i - \frac{M_i}{\sqrt{Y}} \right) = C_X^0 A_i, \quad \frac{1}{2} \left(L_i + \frac{M_i}{\sqrt{Y}} \right) = C_X^0 B_i, \quad N_i = C_X^0 C_i, \quad (\text{A-24})$$

where X stands for ODC and ODCII for $i = 1$ and 2 , respectively.

Appendix 2. Estimation of activation energies for structural recovery

Starting over from Eq. (A-23), we have

$$p + q = \frac{X + \sqrt{Y}}{2} + \frac{X - \sqrt{Y}}{2} = X, \quad (\text{A-25})$$

$$q - p = \frac{X + \sqrt{Y}}{2} - \frac{X - \sqrt{Y}}{2} = Y, \quad (\text{A-26})$$

$$pq = \frac{X + \sqrt{Y}}{2} \times \frac{X - \sqrt{Y}}{2} = K. \quad (\text{A-27})$$

Given that

$$N_1 = \frac{C_{\text{PR}}^0 (C_{\text{STE}}^0 - C_{\text{ODCII}}^0) k_1 k_{-2}}{K}, \quad N_1 = C_{\text{ODC}}^0 C, \quad (\text{A-28})$$

$$k_1 k_{-2} = \frac{C_{\text{ODC}}^0 n_1 pq}{C_{\text{PR}}^0 (C_{\text{STE}}^0 - C_{\text{ODCII}}^0)}, \quad (\text{A-29})$$

and

$$N_2 = \frac{C_{\text{PR}}^0 (C_{\text{IO}}^0 - C_{\text{ODC}}^0) k_{-1} k_2}{K}, \quad N_2 = C_{\text{ODCII}}^0 C_2, \quad (\text{A-30})$$

we have

$$k_{-1} k_2 = \frac{C_{\text{ODCII}}^0 n_2 pq}{C_{\text{PR}}^0 (C_{\text{IO}}^0 - C_{\text{ODC}}^0)}. \quad (\text{A-31})$$

From Eqs. (A-15) and (A-27), we get

$$k_{-1} k_{-2} = \frac{C_{\text{PR}}^0 - C_{\text{ODC}}^0 C_1 - C_{\text{ODCII}}^0 C_2}{C_{\text{PR}}^0 (C_{\text{IO}}^0 - C_{\text{ODC}}^0) (C_{\text{STE}}^0 - C_{\text{ODCII}}^0)} pq. \quad (\text{A-32})$$

Now, k_1 , k_2 , and k_{-2} can be expressed by k_{-1} as:

$$k_1 = \frac{C_{\text{ODC}}^0 C_1 (C_{\text{IO}}^0 - C_{\text{ODC}}^0)}{C_{\text{PR}}^0 - C_{\text{ODC}}^0 C_1 - C_{\text{ODCII}}^0 C_2} k_{-1}, \quad (\text{A-33})$$

$$k_2 = \frac{C_{\text{ODCII}}^0 C_2 pq}{C_{\text{PR}}^0 (C_{\text{IO}}^0 - C_{\text{ODC}}^0) k_{-1}}, \quad (\text{A-34})$$

and

$$k_{-2} = \frac{(C_{PR}^0 - C_{ODC}^0 C_1 - C_{ODCH}^0 C_2) p q}{C_{PR}^0 (C_{IO}^0 - C_{ODC}^0) (C_{STE}^0 - C_{ODCH}^0) k_{-1}}, \quad (A - 35)$$

Then, from Eqs. (A-13) and (A-25), we have

$$\begin{aligned} & C_{PR}^0 (C_{PR}^0 - C_{ODCH}^0 C_2) (C_{IO}^0 - C_{ODC}^0)^2 k_{-1}^2 \\ & + C_{PR}^0 (q + p) (C_{PR}^0 - C_{ODC}^0 C_1 - C_{ODCH}^0 C_2) (C_{IO}^0 - C_{ODC}^0) k_{-1} \\ & + (C_{PR}^0 - C_{ODC}^0 C_1 - C_{ODCH}^0 C_2) p q (C_{PR}^0 - C_{ODC}^0 C_1) = 0. \end{aligned} \quad (A - 36)$$

Eq. (A-36) can be solved as follows:

$$\begin{aligned} (C_{IO}^0 - C_{ODC}^0) k_{-1} &= \frac{-C_{PR}^0 (C_{PR}^0 - C_{ODC}^0 C_1 - C_{ODCH}^0 C_2) (q + p)}{2 C_{PR}^0 (C_{PR}^0 - C_{ODCH}^0 C_2)} \pm \frac{1}{2 C_{PR}^0 (C_{PR}^0 - C_{ODCH}^0 C_2)} \{ [C_{PR}^0 (C_{PR}^0 - \\ & C_{ODC}^0 C_1 - C_{ODCH}^0 C_2) (q + p)]^2 - 4 C_{PR}^0 (C_{PR}^0 - C_{ODCH}^0 C_2) (C_{PR}^0 - C_{ODC}^0 C_1 - C_{ODCH}^0 C_2) p q (C_{PR}^0 - \\ & C_{ODC}^0 C_1) \}^{\frac{1}{2}}. \end{aligned} \quad (A - 37)$$

The terms with the curly brackets can be rewritten as:

$$\begin{aligned} & [C_{PR}^0 (C_{PR}^0 - C_{ODC}^0 C_1 - C_{ODCH}^0 C_2) (q + p)]^2 \\ & - 4 C_{PR}^0 (C_{PR}^0 - C_{ODCH}^0 C_2) (C_{PR}^0 - C_{ODC}^0 C_1 - C_{ODCH}^0 C_2) p q (C_{PR}^0 - C_{ODC}^0 C_1) \\ & = [C_{PR}^0 (C_{PR}^0 - C_{ODC}^0 C_1 - C_{ODCH}^0 C_2) (q + p)]^2 \\ & - 4 C_{PR}^0 C_{ODC}^0 C_1 C_{ODCH}^0 C_2 (C_{PR}^0 - C_{ODC}^0 C_1 - C_{ODCH}^0 C_2) p q. \end{aligned} \quad (A - 38)$$

Considering that $C_{PR}^0 \gg C_{ODC}^0, C_{ODCH}^0$ and given the values of p, q, A_i, B_i in Table 1,

$$\begin{aligned} & [C_{PR}^0 (q + p) (C_{PR}^0 - C_{ODC}^0 C_1 - C_{ODCH}^0 C_2)]^2 \\ & \gg 4 C_{PR}^0 C_{ODC}^0 C_1 C_{ODCH}^0 C_2 (C_{PR}^0 - C_{ODC}^0 C_1 - C_{ODCH}^0 C_2) p q, \end{aligned} \quad (A - 39)$$

then

$$\begin{aligned} & \{ [C_{PR}^0 (C_{PR}^0 - C_{ODC}^0 C_1 - C_{ODCH}^0 C_2) (q + p)]^2 \\ & - 4 C_{PR}^0 (C_{PR}^0 - C_{ODCH}^0 C_2) (C_{PR}^0 - C_{ODC}^0 C_1 - C_{ODCH}^0 C_2) p q (C_{PR}^0 - C_{ODC}^0 C_1) \}^{\frac{1}{2}} \\ & \approx C_{PR}^0 (C_{PR}^0 - C_{ODC}^0 C_1 - C_{ODCH}^0 C_2) (q + p). \end{aligned} \quad (A - 40)$$

Hence, Eq. (A-37) can be rewritten as:

$$\begin{aligned} & (C_{IO}^0 - C_{ODC}^0) k_{-1} \\ & \approx \frac{1}{2 C_{PR}^0 (C_{PR}^0 - C_{ODCH}^0 C_2)} \{ -C_{PR}^0 (C_{PR}^0 - C_{ODC}^0 C_1 - C_{ODCH}^0 C_2) (q + p) \\ & \pm C_{PR}^0 (C_{PR}^0 - C_{ODC}^0 C_1 - C_{ODCH}^0 C_2) (q + p) \}, \end{aligned} \quad (A - 41)$$

which results in

$$(C_{IO}^0 - C_{ODC}^0)k_{-1} \approx \frac{-x(C_{PR}^0 - C_{ODC}^0 C_1 - C_{ODCII}^0 C_2)}{(C_{PR}^0 - C_{ODCII}^0 C_2)}, \text{ or } \frac{-y(C_{PR}^0 - C_{ODC}^0 C_1 - C_{ODCII}^0 C_2)}{(C_{PR}^0 - C_{ODCII}^0 C_2)}. \quad (\text{A} - 42)$$

Since k_2 should be independent of the temperature and q is almost constant, as shown in Table 2, we finally obtain

$$k_{-1} \approx -\frac{C_{PR}^0 - C_{ODC}^0 C_1 - C_{ODCII}^0 C_2}{(C_{PR}^0 - C_{ODCII}^0 C_2)(C_{IO}^0 - C_{ODC}^0)} p, \quad (\text{A} - 43)$$

and

$$k_{-2} \approx -\frac{C_{PR}^0 - C_{ODC}^0 C_1 - C_{ODCII}^0 C_2}{(C_{PR}^0 - C_{ODC}^0 C_1)(C_{STE}^0 - C_{ODCII}^0)} q. \quad (\text{A} - 44)$$

In general, the coefficient k_{-i} ($i = 1$ or 2) for the thermal recovery term has the form

$$k_{-i} = A \exp \frac{E_a}{k_B T}, \quad (\text{A} - 45)$$

where A is the frequency factor, E_a is the activation energy of the recovery event, T is the absolute temperature, and k_B is the Boltzmann constant. The activation energy for the structural recovery can be estimated from the Arrhenius plot.

Appendix 3. Estimation of defect generation rates

Since C_{ODC} and C_{ODCII} are small in the initial stage and the generation terms in Eqs. (A-9) and (A-10) are negligibly small,

$$\frac{dC_{ODC}}{dt} = k_1 C_{PR}^0, \quad \frac{dC_{ODCII}}{dt} = k_2 C_{PR}^0, \quad (\text{A} - 46)$$

then

$$C_{ODC} = k_1 C_{PR}^0 t + C_{ODC}^0, \quad C_{E'} = k_2 C_{PR}^0 t + C_{ODCII}^0. \quad (\text{A} - 47)$$

Since the defect concentrations are much smaller compared to the total concentration of the SiO_4 tetrahedra, C_{PR}^0 ,

$$C_{PR}^0 + C_{ODC}^0 + C_{IO}^0 + C_{ODCII}^0 + C_{STE}^0 \approx C_{PR}^0 = 1, \quad (\text{A} - 48)$$

then

$$C_{ODC} = k_1 t + C_{ODC}^0, \quad C_{E'} = k_2 t + C_{ODCII}^0. \quad (\text{A} - 49)$$

Unfortunately, since the initial CL emission intensities for the defects were normalized to unity and the emission efficiencies were not known, the absolute values of k_1 and k_2 could not be

determined experimentally.

On the other hand, from Eq. (A-22)

$$k_1 = C_{\text{ODC}}^0 \{A_1(1 + pt) + B_1(1 + qt) + C_1\} = C_{\text{ODC}}^0 \{A_1p + B_1q\}t + C_{\text{ODC}}^0. \quad (\text{A} - 50)$$

$$(\because A_1 + B_1 + C_1 = 1)$$

$$\therefore k_1 = C_{\text{ODC}}^0 \{A_1p + B_1q\}. \quad (\text{A} - 51)$$

Similarly,

$$k_2 = C_{\text{ODCII}}^0 \{A_2p + B_2q\}. \quad (\text{A} - 52)$$

Hence, if coefficients k_1 and k_2 are determined theoretically, C_{ODC}^0 and C_{ODCII}^0 can be readily determined based on the fitting parameters in Table 1 and Eqs. (A-51) and (A-52). The C_{ODC}^0 and C_{ODCII}^0 values obtained for the various irradiation conditions should be identical. This would experimentally validate the proposed model.

On the other hand,

$$k_1 = \emptyset \sigma_k^{\text{ODC}} \quad (\text{A} - 53)$$

$$k_2 = \emptyset \sigma_k^{\text{ODCII}}, \quad (\text{A} - 54)$$

where \emptyset is the electron flux and σ_k^{ODC} and σ_k^{ODCII} are the cross-sections for defect formation for the oxygen-deficient defects I and II, respectively. Now,

$$\begin{aligned} \emptyset &= \frac{(\text{experimental current density})}{(\text{electron charge})} = \frac{22.4(\text{A}/\text{m}^2)}{1.60 \times 10^{-19}(\text{C})} \\ &= 1.40 \times 10^{20} (\text{s}^{-1}\text{m}^{-2}) \end{aligned} \quad (\text{A} - 55)$$

and the ionization cross-section, $\sigma_r(E)$, and knock-on damage cross-section, $\sigma_k(E)$, at the incident electron energy E (eV) can be respectively expressed as follows [36]:

$$\sigma_r(E) = \pi \left(\frac{Ze^2}{m_0c^2} \right)^2 \frac{2e^2}{E_{th}^{(r)}\beta^2} \zeta, \quad (\text{A} - 56)$$

$$\sigma_k(E) = \pi \left(\frac{Ze^2}{m_0c^2} \right)^2 \frac{1 - \beta^2}{\beta^4} \left[(\xi - 1) - \beta^2 \ln(\xi) + \pi\alpha\beta \left\{ 2(\xi^{1/2} - 1) - \ln(\xi) \right\} \right]. \quad (\text{A} - 57)$$

where Z is the atomic number of the target atom, m_0 is the electron mass ($= 9.11 \times 10^{-31}$ kg), M_0 is the atomic mass ($M_0^{\text{O}} = 2.66 \times 10^{-26}$ kg, $M_0^{\text{Si}} = 4.69 \times 10^{-26}$ kg), e is the electron charge ($= 1.60 \times 10^{-19}$ C), c is the speed of light ($= 3.00 \times 10^8$ m/s), β is the relativistic correction coefficient ($= \sqrt{1 - (1 + E/m_0c^2)^{-2}}$), $E_{th}^{(r)}$ is the threshold energy for ionization (~ 10.0 eV \sim band gap of SiO_2), and $E_{th}^{(k)}$ is the threshold energy for knock-on damage ($E_{th}^{(k)\text{O}} = 9.30$ eV, $E_{th}^{(k)\text{Si}} = 18.6$ eV). Further, the fine-structure coefficient, $\alpha = Z/137$, $\zeta \approx 10^{-4}$, $\xi = E_{max}/E_{th}^{(k)}$, and the damage energy, $E_{max} = 2E(E + 2m_0c^2)/M_0c^2$.

Since at an accelerating voltage of 100 kV, silicon is not subject to knock-on damage

(energy is below the threshold energy) [36,37],

$$\sigma_r^O = 0.68 \times 10^{-26} \text{m}^2, \sigma_k^O = 0.59 \times 10^{-26} \text{m}^2, \sigma_r^{Si} = 1.18 \times 10^{-26} \text{m}^2, \quad (\text{A} - 58)$$

and at 200 kV,

$$\sigma_r^O = 0.45 \times 10^{-26} \text{m}^2, \sigma_k^O = 0.70 \times 10^{-26} \text{m}^2, \sigma_r^{Si} = 0.74 \times 10^{-26} \text{m}^2, \sigma_k^{Si} = 4.54 \times 10^{-29} \text{m}^2. \quad (\text{A} - 59)$$

Further, since $\sigma_k^{\text{ODC}} = \sigma_k^O + \sigma_r^{\text{Si}}$ and $\sigma_k^{\text{ODCII}} = \sigma_r^{\text{Si}}, \sigma_k^{\text{ODC}}$ at 100 kV

$$\sigma_k^{\text{ODC}} = \sigma_k^O + \sigma_r^{\text{Si}} = 1.77 \times 10^{-26} \text{m}^2 \quad (\text{A} - 60)$$

$$\sigma_k^{\text{ODCII}} = \sigma_r^{\text{Si}} = 11.8 \times 10^{-26} \text{m}^2 \quad (\text{A} - 61)$$

k_1 and k_2 are then estimated by substituting (A-60) and (A-61) into Eqs. (A-53) and (A-54):

$$k_1 = 2.3 \times 10^{-6}$$

$$k_2 = 1.7 \times 10^{-6}.$$

Similarly, at 200 kV

$$k_1 = 2.0 \times 10^{-6}$$

$$k_2 = 1.0 \times 10^{-6}.$$

Tables

Table 1. Peak positions and full width at half maximum (FWHM) values of four Gaussian components in Fig. 2(a).

Component #	1	2	3	4*
Peak (nm)	436	473	535	~640
FWHM (nm)	51	62	110	~59

*#4 consists of multiple Gaussian peaks and values shown are approximate median ones for single component.

Table 2. Fitting parameters of Eq. (5) for components #1 and #2. Values within parentheses are statistical errors of the fit.

E_0 / T	100 kV / 100 K		100 kV / 300 K		200 kV / 100 K		200 kV / 300 K	
Terms	C_{ODC}	C_{ODCH}	C_{ODC}	C_{ODCH}	C_{ODC}	C_{ODCH}	C_{ODC}	C_{ODCH}
$-p$ ($\times 10^{-4}$)	13(2)		36(10)		9.0(0.9)		16(4)	
$-q$ ($\times 10^{-4}$)	4.0(0.6)		4.0(1.2)		4.0(0.5)		4.0(1.5)	
A	-27(1)	-8.0(0.5)	-7.0(0.7)	-3.0(0.5)	-36(1)	-10(0.8)	-15(1)	-5.0(0.4)
B	22(1)	-6.0(1)	4.0(0.5)	-4.0(0.4)	32(0.5)	-0.2(0.3)	8.0(1)	-10(1)
C	6.0(0.5)	15(1)	4.0(0.5)	8.0(1)	5.0(0.5)	11(1)	8.0(0.5)	16(1)

Table 3. Cross-sections estimated based on scheme described in Appendix 3.

E_0 / T	100 kV / 100 K	100 kV / 300 K	200 kV / 100 K	200 kV / 300 K
C_{ODC}^0 ($\times 10^{-4}$)	0.9(0.1)	1.0(0.3)	1.0(0.2)	1.0(0.3)
C_{ODCH}^0 ($\times 10^{-4}$)	1.3(0.1)	1.5(0.4)	1.1(0.1)	0.9(0.3)

Table 4. Fitting parameters (A-C) of Eq. (5) for component #3

E_0 / T	100 kV / 100 K	100 kV / 300 K	200 kV / 100 K	200 kV / 300 K
A	-3.4(0.2)	-1.1(0.1)	-4.3(0.2)	-2.3(0.1)
B	-2.3(0.1)	-1.6(0.1)	-0.08(0.01)	-2.6(0.2)
C	6.7(0.3)	3.8(0.2)	5.4(0.3)	5.9(0.3)

Table 5. Fitting parameters of Eq. (5) for component #4

E_0 / T	100 kV / 100 K	100 kV / 300 K	200 kV / 100 K	200 kV / 300 K
$-p$ ($\times 10^{-4}$)	80(7)	500(40)	200(50)	100(20)
$-q$ ($\times 10^{-4}$)	3.8(0.2)	4.0(0.3)	5.0(0.8)	3.0(0.5)
A	-4.7(0.3)	-0.37(0.2)	-1.4(0.1)	-1.5(0.1)
B	5.0(0.2)	1.2(0.1)	1.7(0.1)	2.2(0.1)
C	0.7(0.1)	0.17(0.2)	0.7(<0.1)	0.3(<0.1)

Figure captions

Figure 1 PL spectra of MPCS samples treated in 0.02-5 M HCl.

Figure 2 (a) Typical CL spectrum of MPCS sample (solid circles); spectrum is deconvoluted into four components (solid lines). See text for detail. (b) High-magnification ADF-STEM image of MPCS, showing honeycomb structure and larger/smaller pores.

Figure 3 Bright-field TEM images and associated CL spectra, showing time dependence of substructure and CL of MPCS sample under electron irradiation (200 keV) at RT. (a)(a') initial, (b)(b') after 50 s, and (c)(c') after 180 s.

Figure 4 Changes in CL intensities for four components in Fig. 2 as function of irradiation time (solid circles). Solid lines are best fitted curves of experimental data and Eq. (5). Accelerating voltage and irradiation temperature are shown inset.

Figure 5 Change in CL profile of non-carbonized MPS sample with electron irradiation (200 keV) at RT. Irradiation time is shown inset.

Figure 6 (a) ADF-STEM image of MPCS sample. (b) Energy-filtered image showing spatial distributions of Si-O (red) and Si-C (green) bonds, generated from the energy regions indicated in (c). (c) Si-L_{2,3} ELNES spectra obtained from framed areas 1 and 2.

Figure 7 Schematic reaction model of defect generation and recovery in silica under high-energy electron irradiation. Pristine (PR) silica is transformed into oxygen-deficient centers (ODCs) and interstitial oxygens (IOs) by knock-on damage process at production rate, k_1 , and recovery rate, k_{-1} . On the other hand, the electron excitation process transforms PR silica into combination of ODCs(II) centers and oxygen pairs, leading to formation of self-trapped excitons (STEs) [26].

Figure 8 Arrhenius plots of recovery rate, k_{-1} (for knock-on damage), at accelerating voltages of 100 and 200 keV.

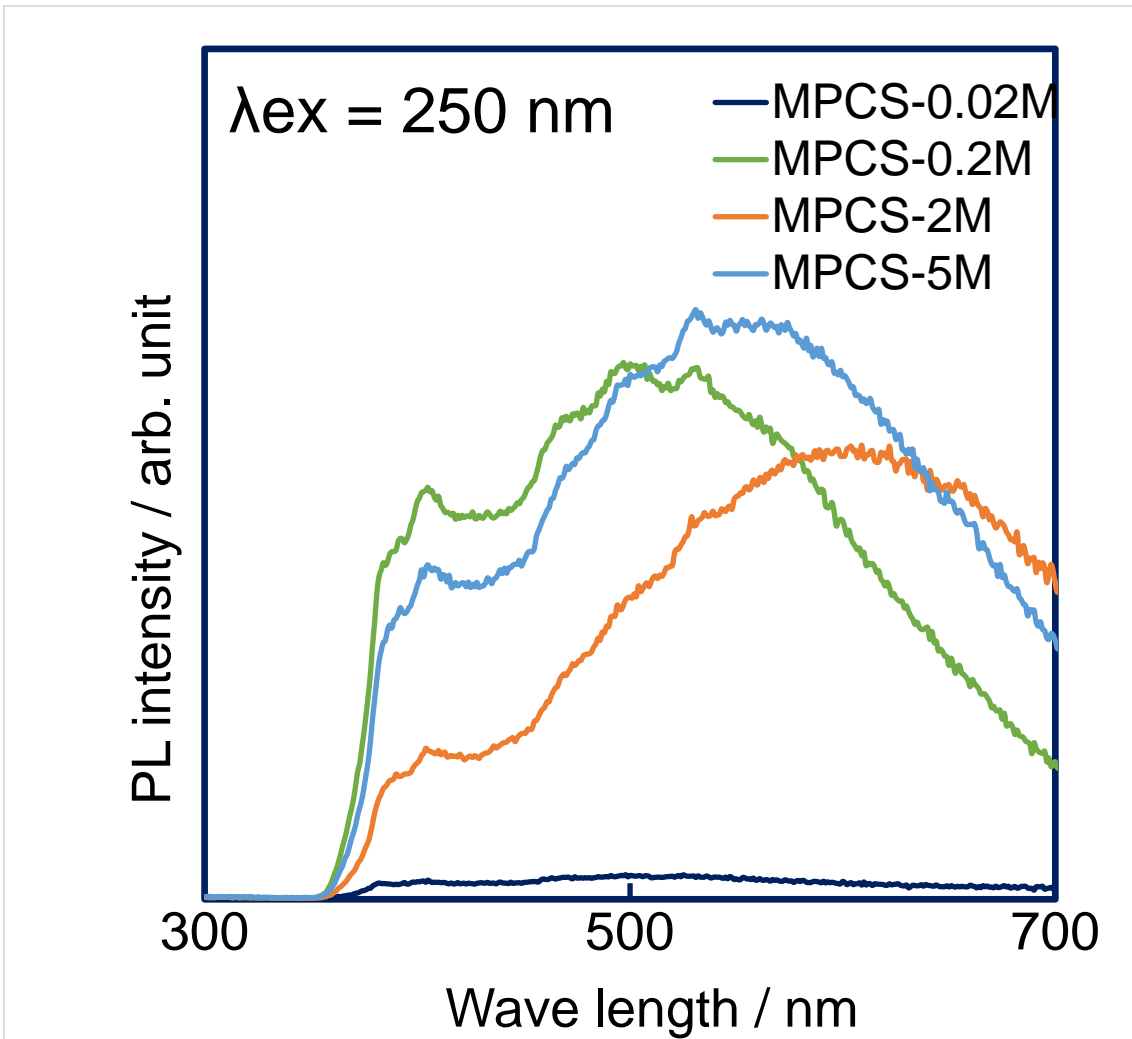


Figure 1 PL spectra of MPCS samples treated in 0.02-5 M HCl.

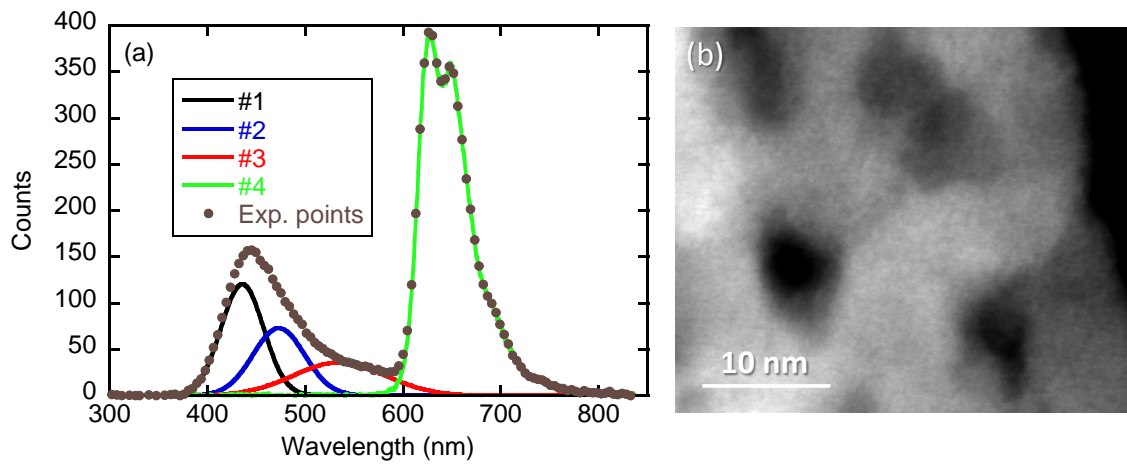


Figure 2 (a) Typical CL spectrum of MPCS sample (solid circles); spectrum is deconvoluted into four components (solid lines). See text for detail. (b) High-magnification ADF-STEM image of MPCS, showing honeycomb structure and larger/smaller pores.

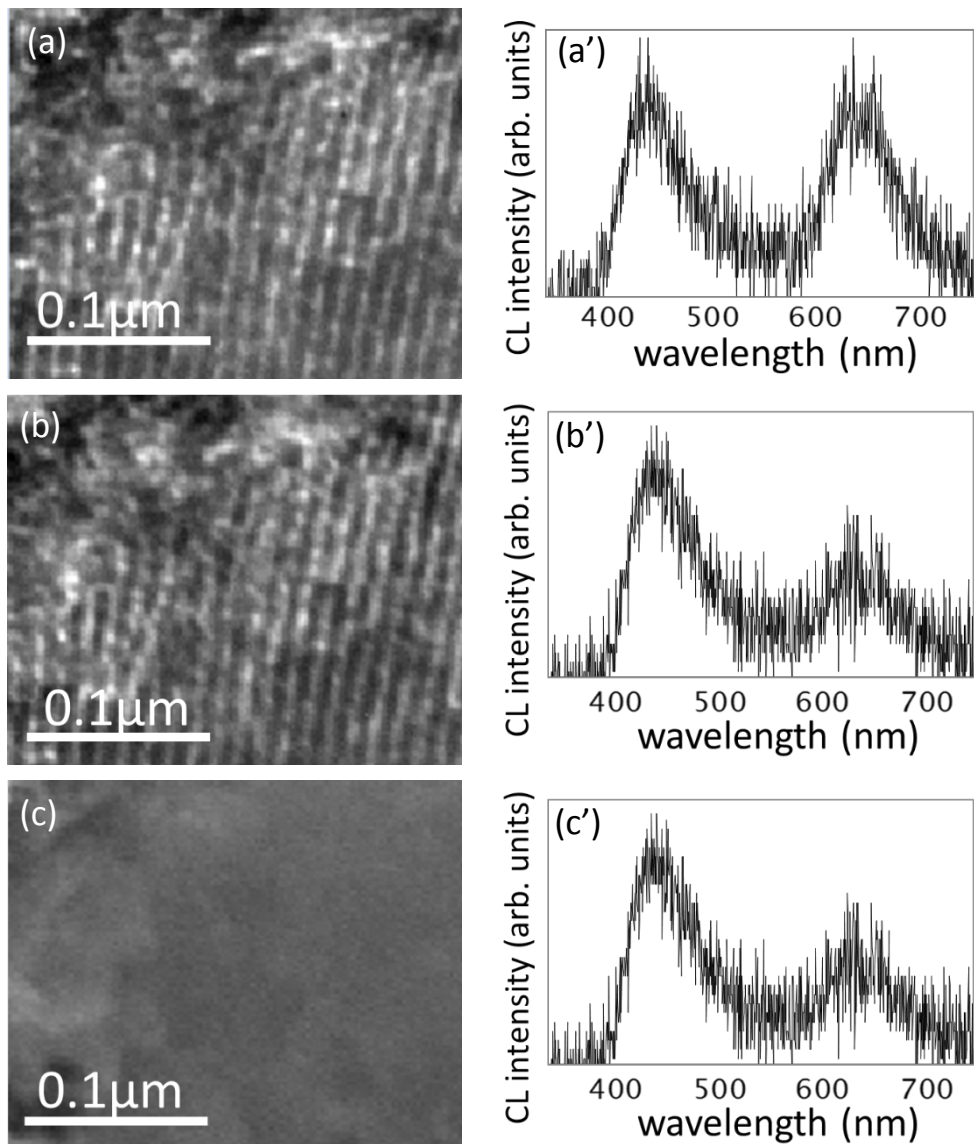


Figure 3 Bright-field TEM images and associated CL spectra, showing time dependence of substructure and CL of MPCS sample under electron irradiation (200 keV) at RT. (a)(a') initial, (b)(b') after 50 s, and (c)(c') after 180 s.

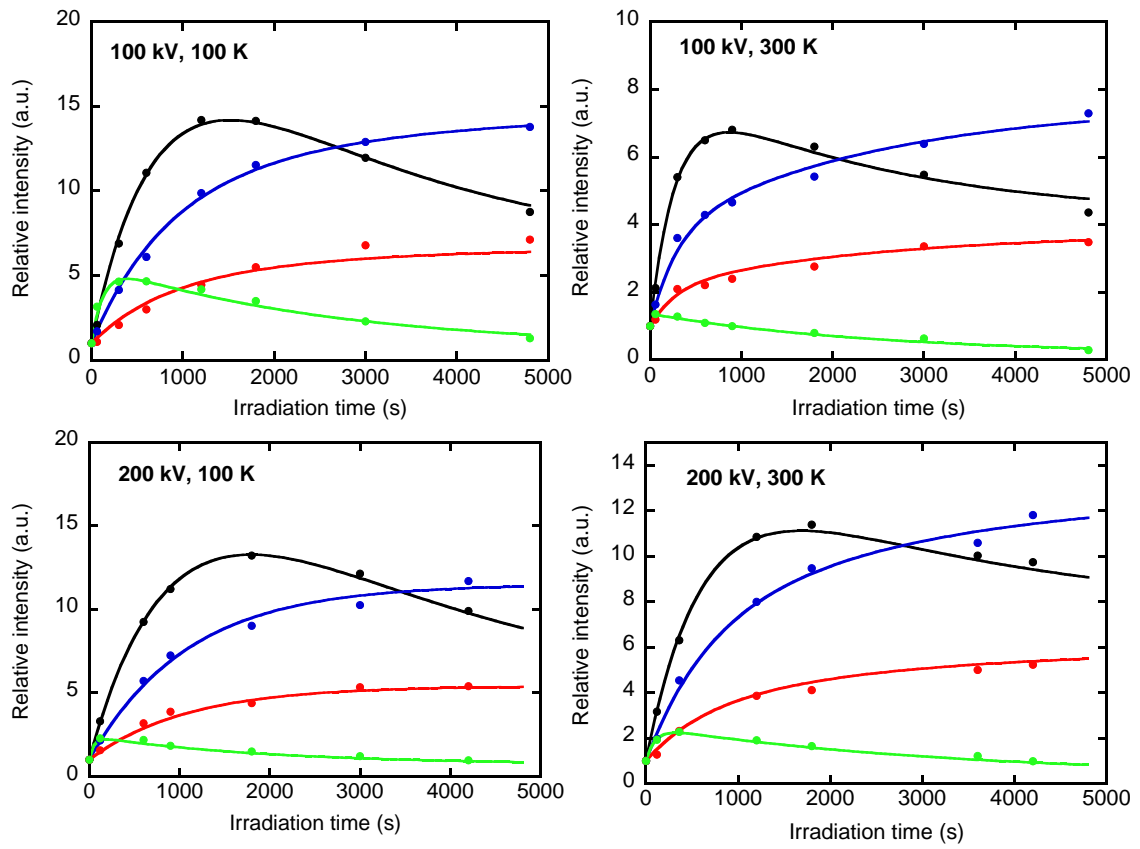


Figure 4 Changes in CL intensities for four components in Fig. 2 as function of irradiation time (solid circles). Solid lines are best fitted curves of experimental data and Eq. (5). Accelerating voltage and irradiation temperature are shown inset.

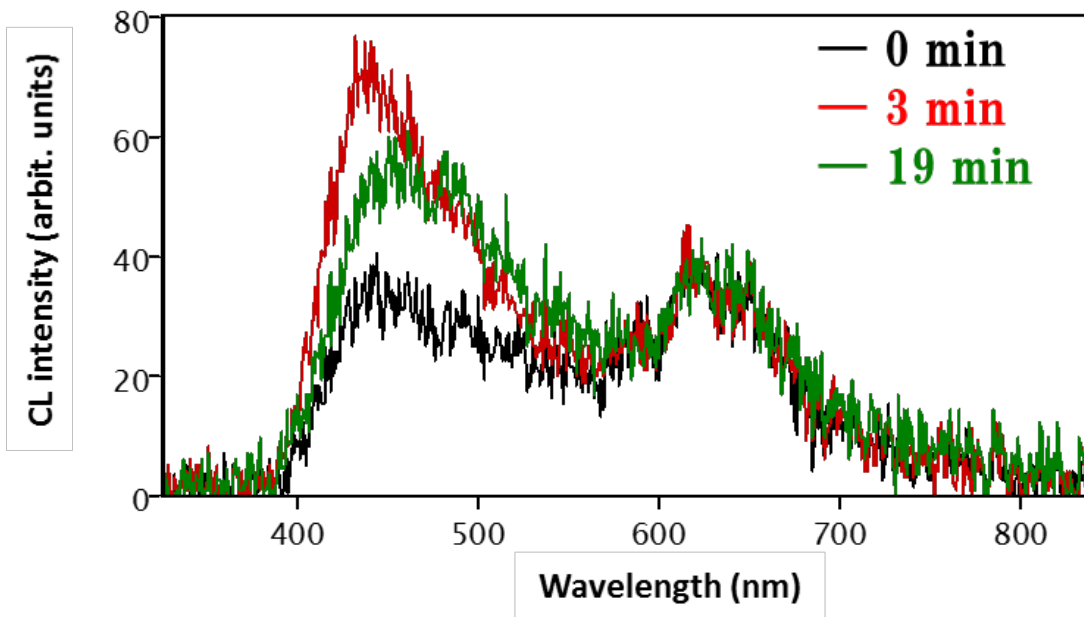


Figure 5 Change in CL profile of non-carbonized MPS sample with electron irradiation (200 keV) at RT. Irradiation time is shown inset.

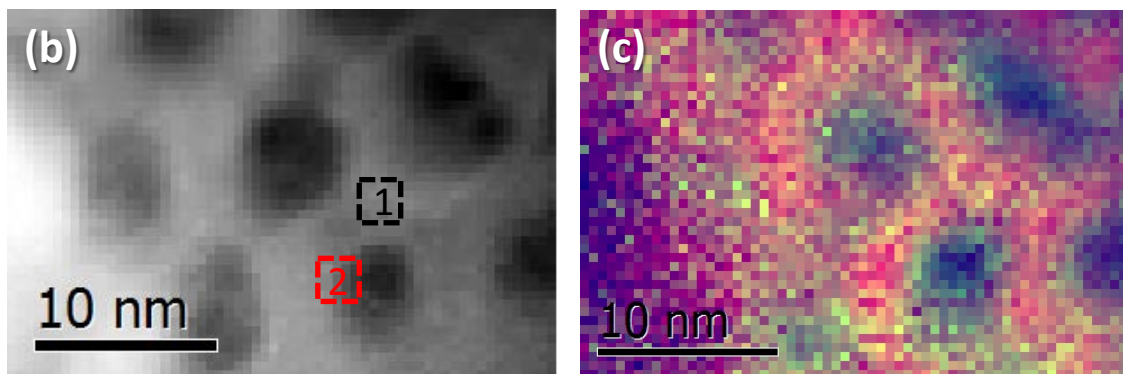
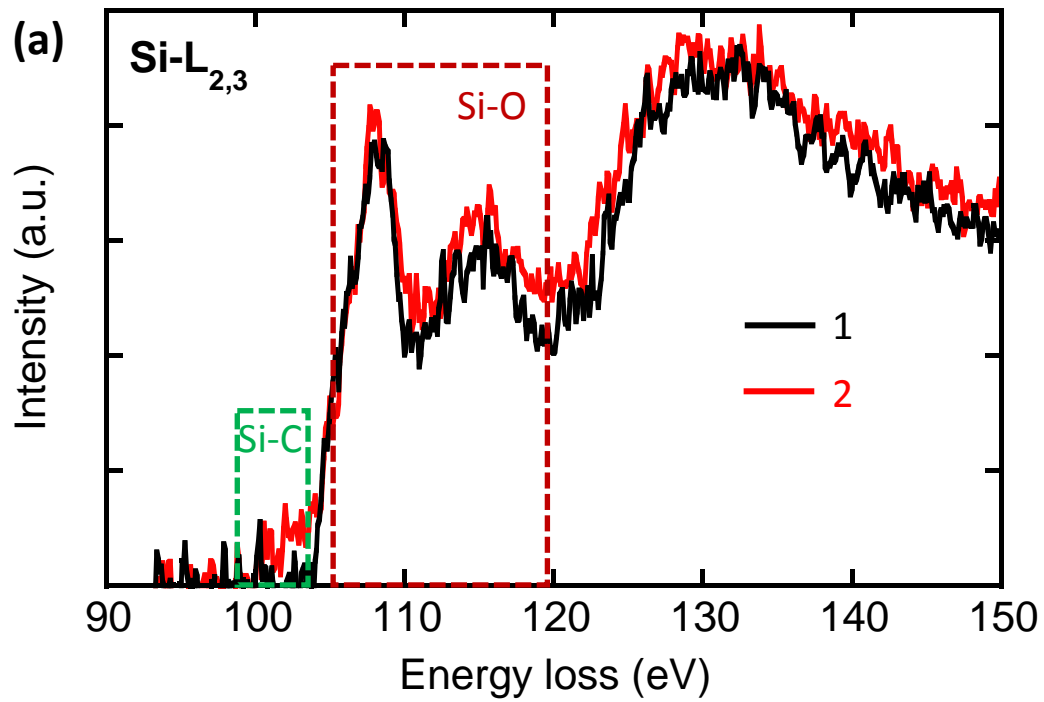


Figure 6 (a) ADF-STEM image of MPCS sample. (b) Energy-filtered image showing spatial distributions of Si-O (red) and Si-C (green) bonds, generated from the energy regions indicated in (c). (c) Si-L_{2,3} ELNES spectra obtained from framed areas 1 and 2.

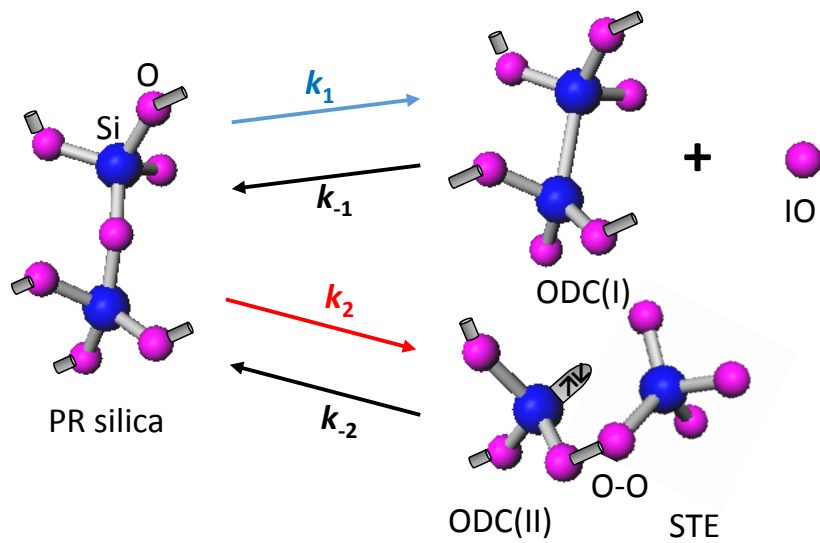


Figure 7 Schematic reaction model of defect generation and recovery in silica under high-energy electron irradiation. Pristine (PR) silica is transformed into oxygen-deficient centers (ODCs) and interstitial oxygens (IOs) by knock-on damage process at production rate, k_1 , and recovery rate, k_{-1} . On the other hand, the electron excitation process transforms PR silica into combination of ODCs(II) and oxygen pairs, leading to formation of self-trapped excitons (STEs) [26].

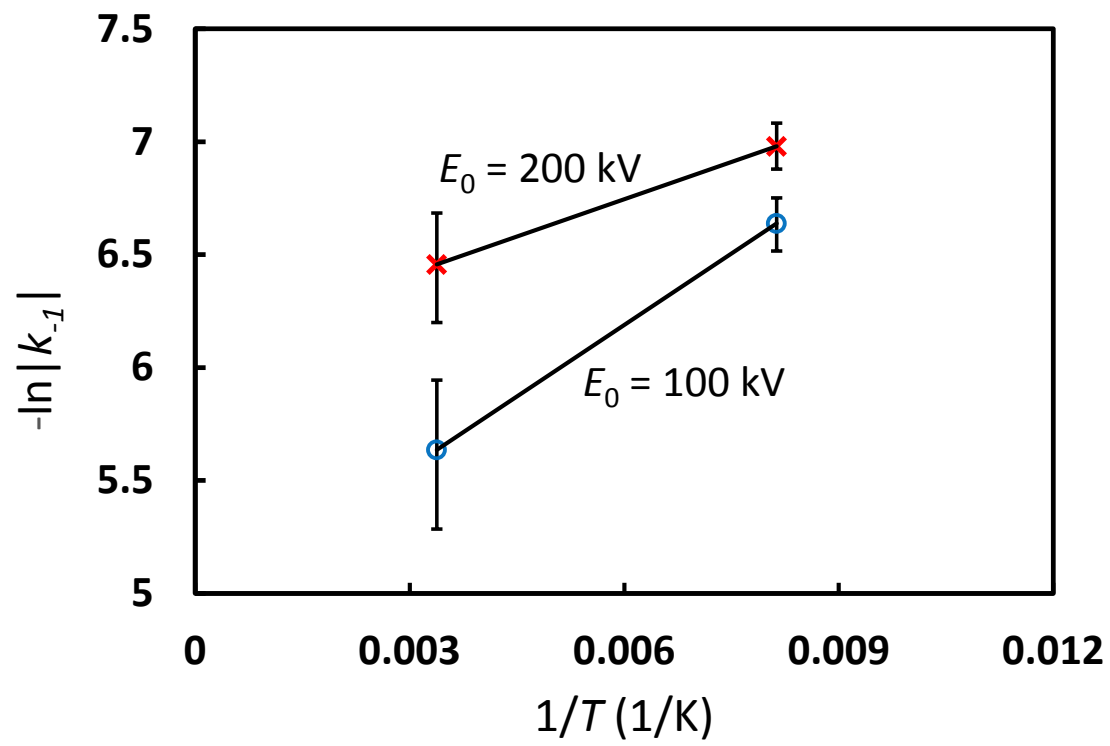


Figure 8 Arrhenius plots of recovery rate, k_{-1} (for knock-on damage), at accelerating voltages of 100 and 200 keV.